Dual-Resonance Dynamic Metasurface for Independent Magnitude and Phase Modulation

Timothy Sleasman,[*,‡] Robert Duggan,[†,‡] Ra'id S. Awadallah, and David Shrekenhamer
Applied Physics Laboratory, Johns Hopkins University Applied Physics Laboratory, 11100 Johns Hopkins Road, Laurel, Maryland 20723, USA

(Received 8 February 2023; revised 11 May 2023; accepted 7 June 2023; published 5 July 2023)

Cascaded dynamic metasurfaces with multiple control points promise augmented capabilities but have received little attention to date owing to complexity in design. The inclusion of multiple control knobs within a single surface offers more degrees of freedom, which can be optimized—jointly with the static geometry—to provide added functionality. We study a cascaded system with two dynamic layers, each possessing patchlike elements that can be tuned with a varactor diode. A resistor is additionally included to add asymmetry in the resonance loss provided by each layer. With this architecture we study the reflection properties of the surface and demonstrate the ability to independently tune the magnitude and the phase from the single, electrically thin surface. Tuning the magnitude and phase separately is a widely sought-after behavior and is used herein to demonstrate multiple communications modulation methods including phase-shift keying and 16-point quadrature amplitude modulation.

DOI: 10.1103/PhysRevApplied.20.014004

I. INTRODUCTION

Metamaterials and metasurfaces have received steady interest over the last two decades, with the maturation of early ideas and the introduction of new concepts continuing to fuel efforts. As more technologies emerge from this ever-branching development process, dynamic metasurfaces have excelled as a promising means to dexterously manipulate electromagnetic waves. While passive metasurfaces have found homes in several applications, e.g., microwave imaging [1] and infrared lenses [2], their dynamic counterparts have been shown to provide added flexibility, enabling them to adapt for situation-specific demands [3,4]. In particular, dynamic metasurfaces, defined by their ability to alter their behavior through an external stimulus, have made great strides in the radio-frequency (rf) spectrum owing to the wealth of possible tuning mechanisms. Further, an abundance of rf applications and technologies are served by the capabilities of dynamic metasurfaces, including reconfigurable intelligent surfaces [5], microwave imaging [6], beam-steering reflectarrays [7], tunable rf lenses [8], wireless power transfer [9], and next-generation adaptive antennas [10,11].

Metasurfaces have chiefly come to the forefront because of their ability to manipulate fields through subwavelength patterning, which allows their electromagnetic responses to be tailored. While early volumetric metamaterials were defined by bulk material properties, a two-dimensional (2D) metasurface is often described as a surface impedance or a collection of polarizabilities or susceptibilities and is substantially easier to accommodate in terms of both modeling and fabrication [12,13]. A hybrid approach also exists where several layers of 2D metasurfaces are cascaded to provide more robust control while avoiding the complications of volumetric fabrication [14]. Cascaded metasurfaces have also delivered the advent of Huygens' metasurfaces, which balance electric and magnetic dipole moments and create a robust physics layer to bring electromagnetic equivalence principles into practice [15].

As cascaded metasurfaces continue to receive attention, there remains ripe opportunity to explore the intersection of dynamic materials with layered metasurfaces. The inclusion of multiple layers intuitively adds degrees of freedom to a metasurface's overall behavior, and yet the question remains how to harness this capability for augmented performance. Here we note that a persistent limitation in the metasurface design process remains how to jointly design the phase and magnitude response of a surface. In instances where a single, passive resonator is utilized in a unit cell, the phase and magnitude are inherently coupled and must be co-designed to satisfy the design constraints. Huygens' metasurfaces overcame this by coupling resonators, but current efforts in this domain fail to provide the agility of dynamic metasurfaces. Given their passive nature, they also are subject to Kramers-Kronig relations, which fundamentally limits their bandwidth performance. The added versatility of a multilayered dynamic

---

[*] timothy.sleasman@jhuapl.edu
[†] robert.duggan@jhuapl.edu
[‡] The first two authors contributed equally to this work.

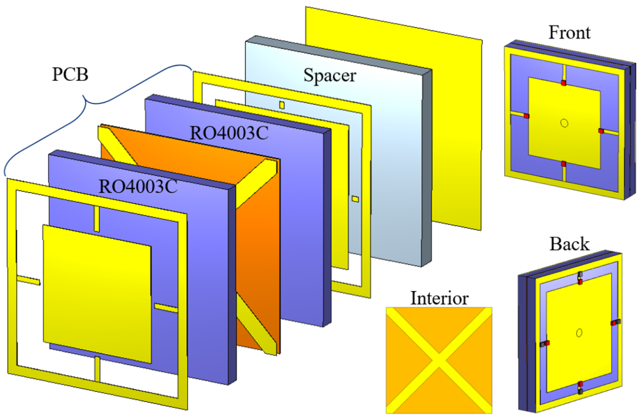

FIG. 1. Dual-resonance unit cell with three copper layers on a printed circuit board and a backplane. The front and back of the unit cell are also shown, which, respectively, host a varactor and series varactor-resistor pair.

metasurface is well suited to address this challenge while maintaining a convenient form factor.

We build on cascaded metasurfaces and dynamic metasurfaces by designing a unit cell that uses two layers and two tunable resonances instead of one (see Fig. 1). The two resonances are separately controlled by two voltage knobs, and, when judicially modified, the separate voltages allow for enhanced control over the surface's magnitude and phase. To provide better control over the reflection magnitude, we include a series resistor into one of the layers. This ultimately enables the ability to modify the reflection phase of the surface without affecting the reflection magnitude (and vice versa). This behavior is favorable for a wide array of applications, e.g., holography and communications, the latter being explored in this work as a demonstration of the surface's capabilities.

Work done by others in this domain includes the development of magnitude-only and phase-only surfaces. A sequential transmission through a magnitude-only surface and phase-only surface thus allows control over the complex transmission coefficient [16]. In Ref. [16] the surface for phase control required two voltages while the surface for magnitude control requires only one, and the combined surfaces were cascaded with an air gap, making the structure an overall thickness of 14.5 mm at 6 GHz, or $\lambda/3.5$. Transmission mode was demonstrated with a loss of -10 dB required to show full 2π phase control. In contrast, the dual-resonance element we propose is $< \lambda/30$ thick, providing a single effective interface (thereby reducing angular sensitivity), and we also require only two control voltages. In another work, the authors achieved independent amplitude and phase control by placing a graphene-electrolyte-graphene sandwich over a traditional metasurface [17]. They show control over the amplitude through the graphene bias and phase through varactors in the metasurface. This approach faces challenges with physical robustness and scaling. Several other designs profess to have their phase and amplitude controlled separately, but these are often passive metasurfaces which do not adapt in real time and which cannot modulate a signal [18–20]. Yet another point of contrast is Ref. [21], where duty cycles are used to present a varied complex amplitude from a binary-tunable surface. In this sense the surface does not create the analog phase and magnitude modulation directly on the incident signal [21], but rather works in concert with a cooperative receiver to deliver complex waveforms that emulate analog modulation.

In this work we begin by designing and simulating a dynamic cascaded metasurface with the intent of independently controlling reflection magnitude and phase. Within the constraints of printed circuit board (PCB) technology, we show that being able to tune two appropriately designed layers independently gives the knobs we need. Specifically, by changing only capacitances in the system (achievable with varactors), some in series with resistors, we can continuously control the resonance and loss of both fundamental modes in the system. Of particular interest is how modification of these resonances results in variation of the reflection magnitude and phase of the surface, and how the parameters of the surface's constituent components are adjusted to provide the desired response. These considerations are further elucidated through demonstrations with a coupled-mode theory model. We then fabricate and experimentally characterize the metasurface with two voltages, measuring all combinations and showing the possibility to tune the phase while maintaining a constant magnitude over a wide band of incident frequencies. Then we demonstrate the utility of the metasurface in a communications environment by encoding bits on an incident signal with different modulation methods. Finally, we conclude by articulating some interesting avenues for continued development and discussing applications where the dynamic cascaded metasurface may find use.

II. CASCADED DYNAMIC METASURFACE ELEMENT WITH DUAL RESONANCES

A. Design considerations

Dynamic metasurfaces have played an increasingly important role in recent years as their passive counterparts have improved to be near to the point of diminishing returns. Across the electromagnetic spectrum several approaches toward adaptive behavior have been pursued, with the most successful results at rf wavelengths being found through commercial-off-the-shelf (COTS) semiconductor components. Options include *p*-*i*-*n* diodes, varactors, and transistors, each providing different pros and cons such as power consumption and control plane complexity. Varactors have proven to be particularly interesting devices and are implemented here since they provide grayscale tuning by changing the applied voltage (which in turn tunes the capacitance) and draw minimal current (enabling large arrays at high frequencies). One consequence of using varactors is the difficulty in applying a continuously tunable voltage to individual elements [22] or subpixels [23]. Instead of attempting element-level addressability, we tune the entire surface in parallel, with the expectation that more sophisticated biasing networks [7,24] can be constructed if spatial control over the metasurface becomes desirable.

Metasurfaces often exhibit their most interesting behavior around the resonance of their subwavelength metaelement geometry. As such, the capacitance variation that results from varactor tuning is manifest through modification of the resonance frequency, often taking the form $\omega_0 \sim 1/\sqrt{LC}$. Common models for this are seen in elements with Lorentzian dipolelike behavior [25,26] as well as mushroomlike artificial impedance surface elements [27,28]. In either case, the resonance occurs where greater surface currents or displacement currents arise, and therefore the mode will inherently have increased loss that is peaked at the resonance. If variable phase is desired, the resonance can be shifted but with the deleterious side effect that the magnitude will also be impacted. In the case where COTS components are utilized, the enhanced currents often cause non-negligible loss in the varactor itself, creating further magnitude variation.

Given the inherent restrictions of lossy, single-resonance metasurfaces, we pursued a design with two resonances and two biasing degrees of freedom. We adopt an element akin to the artificial impedance surfaces pioneered by Sievenpiper *et al.* [27,28], but with the modification that two patches (with two different resonance) will be stacked and separately tuned. The traditional single-patch mushroom structure exhibits a resonance that progresses through 2π reflection phase, with perfect magnetic conductor (PMC) behavior at resonance and perfect electric conductor (PEC) behavior when sufficiently above or below resonance. When two resonant modes are created with slightly different frequencies, the effects of the resonances compound. Where the spectral response is dominated by the first (second) mode, the reflection response is primarily governed by the first (second) mode, and in between the effects of both modes are felt. In our case, the two modes will be independently tunable, in contrast to many other works where a single component or voltage modifies multiple resonances [29]. Such designs often seek to hybridize multiple resonances to create binary phase switching over a wide bandwidth whereas our two resonances can be controlled independently.

Because our surface will consist of two metasurfaces in a subwavelength thickness, transmission-line theory has been shown to be a valid approximation [30,31]. Each metasurface layer is effectively a shunt series *RLC*, with transmission lines connecting the various layers of the system. However, while simpler than full-wave simulations, the transmission-line model leads to complicated transcendental equations for the coupling coefficients, and even still misses some effects like evanescent coupling between metasurface layers unless more complicated models are used [32]. Instead, we can abstract even further and use coupled-mode theory (CMT) [33,34], which has been widely used to study systems dominated by a few resonant modes. While some of the details are lost in this framework, it gives insights into the interplay between resonance frequencies that generalize beyond our specific unit-cell design and even into other domains of wave physics.

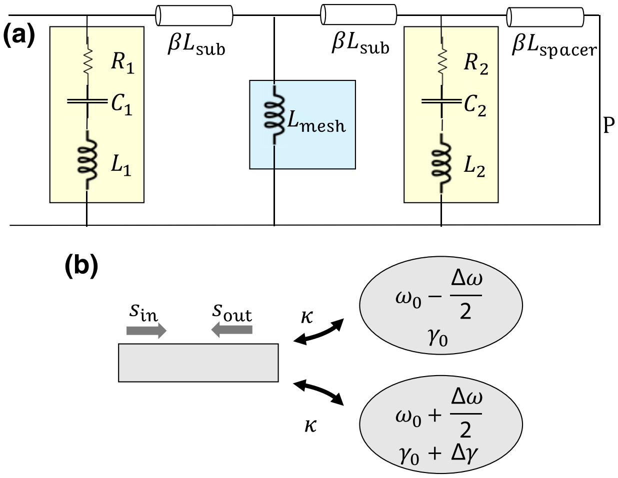

FIG. 2. Simplified models of the multilayer metasurface. (a) Transmission-line model. The two tunable layers (highlighted in yellow) act as shunt *RLC*s, the middle metallic layer (blue) is a shunt inductance, and the layers in the PCB and spacer serve as transmission-line segments. (b) The CMT model we used is two resonances independently coupled to the incident wave, each with a characteristic resonance frequency and absorption loss. For Fig. 3, we used $\kappa = 1$.

A model for our metasurface (Fig. 2) is two resonances that independently couple to the plane-wave radiation with strength κ, and have their own resonance frequency ($\omega_0 \mp \Delta\omega/2$) and absorption rates ($\gamma_0$ and $\gamma_0 + \Delta\gamma$), respectively. The term $\Delta\omega$ captures the difference in resonance frequencies between the two modes, and $\Delta\gamma$ accounts for any difference in absorption. We acknowledge that this is a simplified model that misses some effects, such as direct coupling between layers and phase accumulation through the substrate, for the sake of a simplicity and building intuition. The reflection coefficient can be calculated per the approach in Ref. [34].

We can see the effect of various system parameters by adding contributions from each of the above parameters one by one. We plot representative results in Fig. 3, which show the reflection phase and amplitude values achievable within a given range of parameters. When $\Delta\omega = 0$ and $\Delta\gamma = 0$, the system acts like a single resonance. As ω_0 is varied relative to the incident frequency ω, the reflected

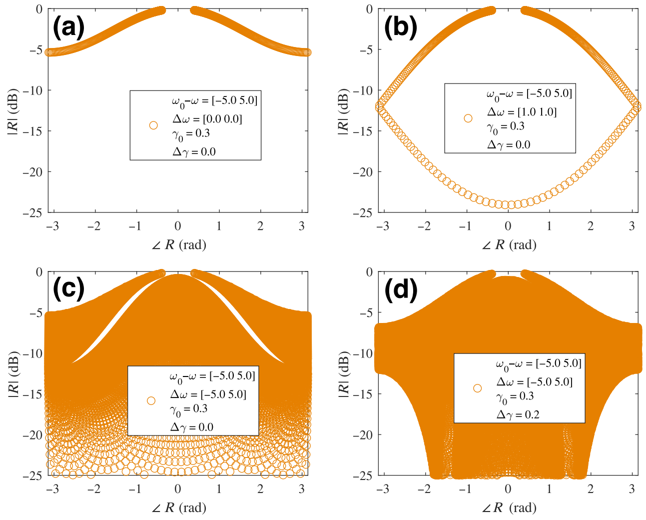

FIG. 3. Available reflection coefficients using CMT. Values for free parameters are included in the panel legends. (a) Tuning only a single resonance frequency. (b) Tuning two resonances while keeping a fixed frequency difference. (c) Tuning both resonances independently. (d) Tuning both resonances with a fixed absorption difference between them.

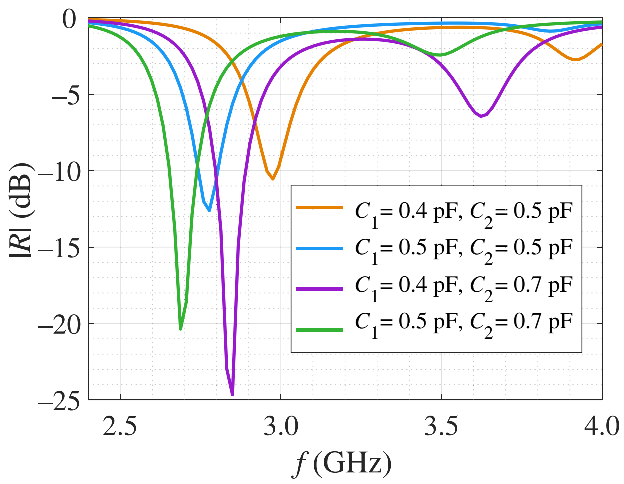

FIG. 4. Simulated scattering parameter for the proposed unit cell at four bias states.

signal undergoes a phase shift, but also an amplitude dip from passing through resonance. There is still a one-to-one relationship between amplitude and phase, however. When a constant $\Delta\omega$ is introduced and ω_0 is again varied, there is now effectively an almost 4π phase shift, so that, for each reflection phase, there are generally two amplitude points. If the two resonant frequencies can be independently tuned, a solid area of the complex reflection map fills in, including some amplitude bands where a full 2π of phase is available. Finally, we add more absorption to the second mode, and again vary the two resonances independently. In this case, the maximum amplitude where full phase coverage is available actually *increases*.

With these insights, in our approach the second layer (second patch) is still varactor-tuned, but in addition we include a resistor in series with the varactor. For a resistance in series with a capacitance, as the capacitance increases, not only is there a redshift of the resonances, but also current flows more freely through the resistor under rf illumination. This in turn increases the power dissipation for a given voltage. In contrast with a *p*-*i*-*n* diode, which can be switched discretely between conductive and resistive states, utilizing a varactor-resistor series combination allows a continuous tuning of the effective losses, although it is still not completely decoupled from the resonance shift, unlike the CMT section above. The additional resistance increases the relative change in loss compared to the induced resonance shift by the capacitance change, allowing more control over the amplitude.

Figure 4 shows the behavior of the final unit cell, which we will more fully explain in Sec. II B. Since we have two dynamic layers, there are two resonances in the system that can be tuned. Increasing C_1 generally redshifts resonances, with a slight effect on the amplitude. Increasing C_2, which has an additional resistance in series, also redshifts resonances, but also results in a much larger effect on the amplitudes. All of the curves in Fig. 4 are in the underdamped regime, such that increasing the effective losses brings the system closer to critical damping. Eventually, the dissipation will be excessive (overdamping), and increasing effective losses *reduces* absorption. Being able to tune through underdamped and overdamped conditions for a resonance at a given frequency generally gives the ability to cover a wide range of phases up to a certain maximum amplitude.

The designed element is shown in Fig. 1. Each dynamic layer consists of a square patch at the center of the unit cell and a thin metallic mesh around the perimeter of the cell. The mesh and patch are connected on each side with thin metal strips in line with a varactor. The second layer also has a lumped resistor added between the strips and the mesh. The bias voltage between the mesh and the patch determines the effective capacitance of the varactor, and thus modifies the resonance properties of the unit cell. Note that, since the varactors are always in reverse bias, there is minimal steady-state current flow through the resistor from dc biasing voltage. In between the two dynamic layers, separated by dielectric, there is a metallic grid rotated 45°, with the intersections aligning with the center of the patches on either dynamic layer. The patches are then connected to this middle layer by vias. This sets a common ground for the biasing network. Finally, a spacing layer separates the whole engineered structure from a metallic backplane.

B. Simulation

Simulations of the dual-layer metasurface were performed with the COMSOL Multiphysics [35] frequency-domain solver. Lumped series *RLC* elements were used in the place of varactors (SMV2019-040LF), and an additional lumped resistor was used in the second layer as described above. Metal layers were modeled with copper properties, the PCB dielectric between the metaelement, and crisscross layers with 1.5 mm Rogers 4003C ($\epsilon_r = 3.55$), and the spacer to the backplane with 2 mm of Teflon-like $\epsilon_r = 2.2$. All simulations were performed with normally incident plane waves, imposed with appropriate PEC boundary conditions on one set of opposing unit-cell faces and PMC on the other.

Simulations served to confirm the concept at an initial design frequency, and then an iterative approach was taken with the unit-cell dimensions and lumped resistor value to improve the range of operational frequencies with 2π phase coverage at a fixed amplitude. These results are subject to the given range of capacitance values achievable with the varactors (0.30–2.22 pF). For a fixed unit-cell shape, there is a limit to how much the frequencies can shift given the capacitance range of the varactors. There is also a limit set by losses in the system, particularly with the addition of the lumped resistor. If the resonance becomes overdamped, it will not be sufficiently excited to provide the full phase coverage. From our simulations, the overdamping tends to set the upper frequency of operation. As the unit cells get electrically smaller, they radiate less efficiently, and the absorption dominates.

Our final design consists of a 2Ω resistance added in series with the varactors in the second layer. Note that this is roughly half of the intrinsic resistance of the diode (4.8Ω). The patch is also slightly larger in this layer, which serves to make this layer resonate at a higher frequency. This is because the resonance frequency is actually set by the lengths of the strips between patches rather than by the resonance of the patches themselves. Simulation results indeed match the expected behavior. As the capacitance of the second layer (C_2) is increased, more current flows through the extra resistor and the loss at resonance increases to the point of reaching critical damping (perfect absorption) and then overdamping (phase going through zero instead of wrapping around $\pm\pi$). Increasing C_2 also redshifts the resonance slightly. The system can be brought back on resonance by then decreasing the capacitance in the first layer (C_1), as shown in Fig. 5. Through tuning both capacitances, a wide area of complex reflection coefficient space can be covered, which is in stark contrast with the single-resonance surface, which can achieve only a single curve through complex space.

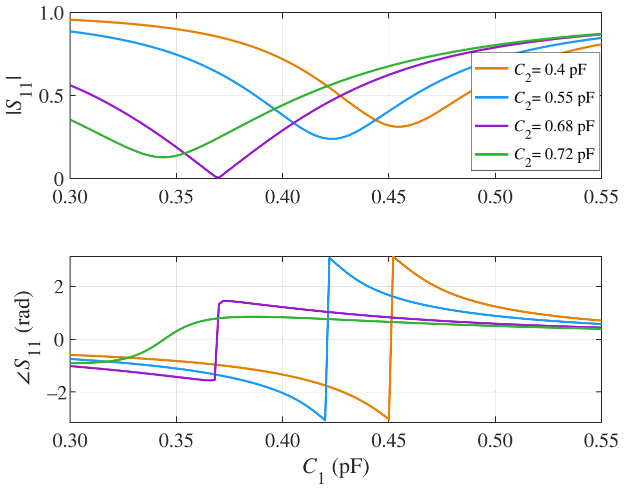

FIG. 5. Simulated scattering parameter for the proposed unit cell at 2.9 GHz.

Note that Fig. 5 is for a fixed frequency and each line represents a fixed value of C_2. This is a subset of a more complete $[C_1, C_2]$ space where both are continually varied. Since there is a direct relationship between the varactor's capacitance and the applied voltage, we can make a $C \to V$ conversion with the information from the diode data sheet in order to better compare with our experimental results in Sec. III. Figures 6 and 7 show the phase and amplitude maps of the reflection at 2.9 GHz and 3.4 GHz, respectively. These maps have been interpolated since the full-wave simulations are time-consuming and combinations C_1 and C_2 accumulate quickly.

When the system can be brought to a critical coupling point in $[V_1, V_2]$ space, tracing a curve around this point comes with a 2π phase wrapping. Numerous contours can be followed at different fixed amplitudes. In our simulation results, there is one resonance (reflection null) that can be fully encircled with full phase coverage within the available capacitance values in the ~ 2.5–3 GHz range (shown at 2.9 GHz in Fig. 6). At ~ 3 GHz, hitting this null requires a $V_2 > 20$ V, outside the range of our varactors. At slightly higher frequencies, the second resonance null starts to enter the available space at the lower

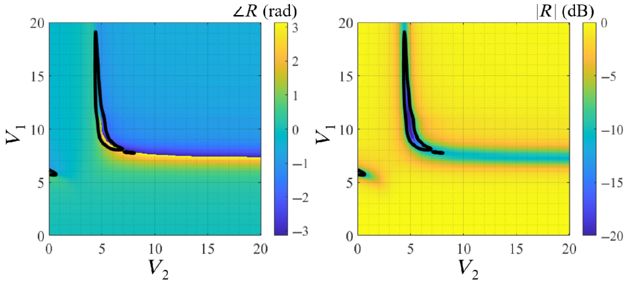

FIG. 6. Phase and amplitude of reflection coefficients at 2.9 GHz by varying C_1 and C_2. The black contours indicate the maximum value of amplitude where full phase coverage can be achieved.

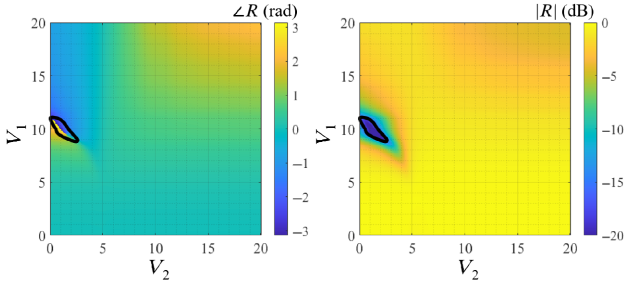

FIG. 7. Same plots as Fig. 6 for 3.4 GHz. A second mode for small V_2 (large C_2) appears.

V_2 voltage. The second null is visible for the 3.4 GHz maps in Fig. 7. This resonance provides full phase coverage for ~ 3.3–3.8 GHz. Each resonance thus provides an opportunity for full phase coverage over a frequency band. In between these bands, neither resonance can be completely encircled, but the interaction between them still allows for coverage over a wide range of phase values, though not complete control at a fixed amplitude.

While the $[V_1, V_2]$ maps are useful for understanding the physics of the metasurface, the question of coverage in phase or amplitude space is not obvious. An alternative data representation ignores the voltage dependence and plots only the available amplitude as a function of phase. These scatterplots are shown for the same two frequencies in Fig. 8. Interpolation was utilized to densely fill this map, and in locations where a dense collection of points are available the map fills to become solid. It is likely that more interpolation will continue to fill the map—ultimately the limit of this approach will depend on the resolution of the voltage source. There is very clearly a set of simulation points in Fig. 8 that span the full phase span at about −10 dB. For the higher frequency, this amplitude is decreased to −16 dB, but there is also indication that another band is forming near −5 dB. This result is included for later comparisons with experimental data which show similar performance in Sec. III.

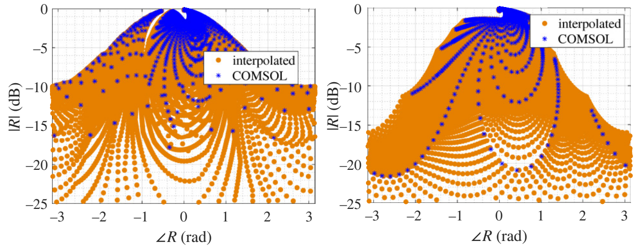

FIG. 8. Simulation of available reflection coefficients at 2.9 and 3.4 GHz by varying C_1 and C_2. The blue asterisks indicate results from COMSOL, and the orange circles are the results from splining the simulation results onto the equivalent of a 0.05 V grid.

In addition to simulations run at normal incidence, the angular resilience of the design was studied in simulations at oblique angles up to 30°. At the lower portions of the bandwidth, the performance is retained for both transverse electric (TE) and transverse magnetic (TM) polarizations. Near the top of the band the performance is more sensitive—particularly for TM polarization—and performance shows non-negligible variation at 20°. Determining the impact of this variation is application-specific and is therefore left to future work where a specific performance metric can be evaluated. However, it is worth noting here since the experiments have a small angle of incidence that is not reproduced in the shown simulations.

III. EXPERIMENT

The element simulated and depicted in Fig. 1 was fabricated via standard PCB processes and is shown in Fig. 9. A 1-mm-thick silicone spacer was used and the board was mounted to a rigid, metallic superstrate. The total thickness was thus 2.5 mm. While the substrate thickness and properties are not an exact match to the simulation, the properties are fairly close and are not expected to cause substantial variations. Any minor frequency shift from the simulation can therefore be attributed to the spacer characteristics, differences between the mounted diode and the idealistic data sheet, or fabrication tolerances from the PCB manufacturing. Fabrication robustness and manufacturing considerations are not expected to be a substantial concern for this technology based on the heavily optimized nature of PCB fabrication for comparable technologies. The greatest model inaccuracy for the present prototype is expected to be the silicone spacer since it does not have controlled rf material properties. In realistic manufacturing, diode variation could become a limiting factor, but the results presented below show that these considerations are not overly concerning at the presented frequencies

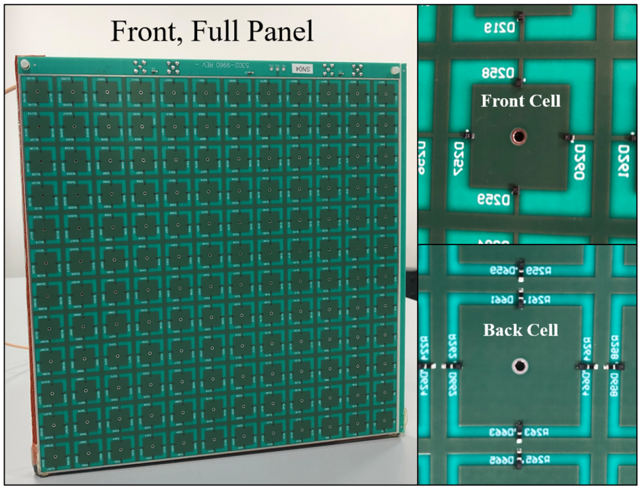

FIG. 9. Picture of the fabricated metasurface as a full panel as well as front and back views of the unit cell.

(though they may become more temperamental at higher frequencies).

A. Characterization

The first experiment conducted was a quasimonostatic specular reflection measurement with a vector network analyzer (VNA). Measurements took place in an anechoic chamber to mitigate noise and multipath reflections. Two ultrawideband horns were utilized, one for transmit and one for receive, separated by ∼ 1 m. The metasurface was placed at a distance of ∼ 3 m. Direct horn-to-horn coupling and reflections from the walls of the chamber were found to be below the primary reflection of interest by ∼ 30 dB. With the VNA, these signals are time-gated and the noise floor is substantially lower (> 50 dB), but in the subsequent communications demonstration this sets the effective dynamic range of the system.

Two power supplies were utilized to independently control the two different layers of the cascaded metasurface. The varactors had a maximum bias voltage of 20 V and measurements were taken for the range 0–19.95 V with a step size of 0.15 V. This step size was found to be fine enough to interpolate, as discussed in Sec. III B. It should be noted that, while a linear step size was utilized for the voltage, this does not correspond to a linear map in capacitance and the results observed tend to saturate beyond 15 V where the diodes' capacitance has minimal variation.

Magnitude and phase maps are shown in Figs. 10 and 11 for frequencies 2.9 GHz and 3.4 GHz, respectively. The magnitude in each map is normalized to the case when $V_1 = V_2 = 0$ V, where the resonance is far from the measurement frequency and the metasurface presents as a PEC plate. While similar, these two maps show the effects of the two resonances, as was seen Figs. 6 and 7. Phase wrapping discontinuities are seen where the resonance occurs in the $[V_1, V_2]$ map, with the two different frequencies highlighting the effects of each resonance (with minor perturbation of the other resonance). The resonance is seen to create enhanced loss, as discussed in Sec. II. Notably, there exists a rich collection of phases (spanning the entire $-\pi$ to π range), along with magnitude variation when a fixed phase is selected.

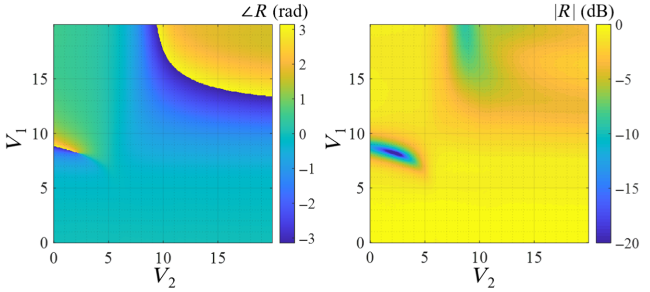

FIG. 11. Maps of the experimentally measured phase and magnitude at 3.4 GHz.

For comparisons with simulations and to show the magnitude as a function of phase, we also plot scatter maps in Fig. 12 (simulation shown in Fig. 8). Both frequencies show that it is possible to cover the entirety of phase space while maintaining a constant magnitude. In the case of 2.9 GHz, this can be accomplished with a reflection loss of −11 dB, while at 3.4 GHz the resonances create a band at −4 dB where a near-constant magnitude can be maintained. Phase coverage at −11 dB and below is also accomplished. Complete phase coverage may be essential for some applications, while other instances will require only a discrete number of phase points, e.g., binary phase-shift keying (BPSK). In the latter case, it is likely that the loss will not be so severe. Additionally, we expect that some loss can be mitigated by using alternative varactors which are not currently available in large numbers.

Coverage of the entire phase space is only strictly available across a given bandwidth. Additionally, the amplitude at which phase coverage is satisfied is frequency-dependent. To quantify this operational bandwidth, we track which frequencies allow full phase-space coverage with minor amplitude variation. This variation can be denoted "tolerable magnitude imbalance" (TMI) and will be different for each frequency and magnitude level. The analysis of the bandwidth performance (for a given magnitude and TMI) is shown in Fig. 13. As an example,

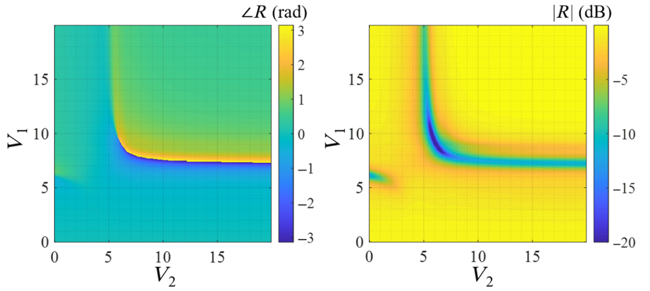

FIG. 10. Maps of the experimentally measured phase and magnitude at 2.9 GHz.

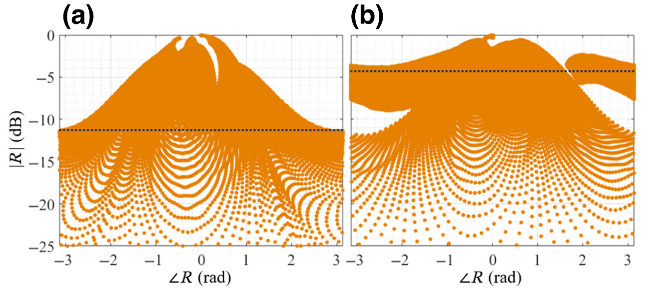

FIG. 12. Scatterplots that show the magnitude and phase coverage for frequencies (a) 2.9 GHz and (b) 3.4 GHz.

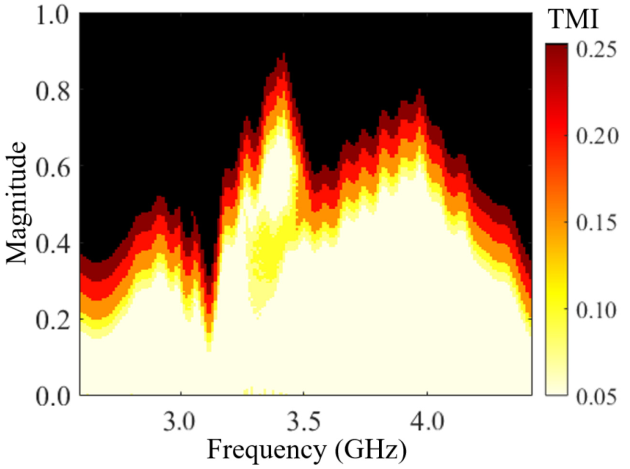

FIG. 13. Bandwidth for which a balanced amplitude can be achieved. The color indicates how much magnitude imbalance can be tolerated. Locations in black do not support full phase coverage.

at 3.4 GHz, when the desired magnitude is 0.67 (−3.5 dB), the complete phase coverage can be obtained if the magnitude is allowed to vary by ±0.05 (between 0.62 and 0.72). This corresponds to the line drawn in Fig. 12. It can be seen that, at the slightly lower magnitude of 0.37 (−8.6 dB), a variation of 0.1 must be tolerated.

Figure 13 shows that there is reasonable performance between 2.5 GHz and 4.5 GHz, but also highlights that a subset of these frequencies will have improved magnitude performance. In instances where a subset of the phase space is required, this performance is likely an underestimate. For example, if operating with quadrature phase-shift keying (QPSK), it is unnecessary to cover the entire phase space, and the magnitudes associated with the phase points that are found may be substantially larger than shown in Fig. 13. On the other hand, 16-point quadrature amplitude modulation (16-QAM) requires quadrature phase and *multiple* amplitude levels, and therefore may have worse performance than shown in Fig. 13 (since the result is shown for a single magnitude level). Such assessments can be optimized on an as-needed basis.

It should be noted that, while this analysis demonstrates an operational bandwidth, the applied voltages are frequency-dependent and therefore the instantaneous bandwidth will be significantly reduced. Fortunately, communications channel widths tend to be on the order of megahertz and at these small scales the voltage is slowly varying.

B. Communications demonstration

After collecting the static reflection coefficients over the $[V_1, V_2]$ map, we added a temporal modulation to demonstrate encoding of common communications waveforms. While communications is not the only relevant scenario, it serves as an interesting testbed to show how magnitude and phase can be independently controlled. Other applications are discussed in Secs. I and IV.

When progressing to modulation experiments with waveforms varying on the microsecond time scale, a minor reconfiguration of the experiment is required. The VNA, previously serving as both transmitter and receiver, is replaced by a signal generator (and amplifier) on transmit and an oscilloscope (and hybrid coupler for in-phase and quadrature separation) on receive. The power supply is replaced by an arbitrary waveform generator (AWG) to enable synchronized rapid voltage modulation on the two layers. The signal generator created a continuous-wave tone at 2.8 GHz. This frequency is not optimal because it was chosen before rigorous analysis was complete, but the results are representative of behavior throughout the operational bandwidth. Better performance through improved signal-to-noise ratio can be found in the range 3.2–4.2 GHz, but this is left to future study where measurements will be devoted to demonstrating the limits of communications performance with the proposed technology.

To modulate symbols onto the carrier signal, the metasurface is given desired complex amplitudes, which correspond to coordinates in the $[V_1, V_2]$ plane. To fill in the data space between the measured static data points, we performed a 2D cubic interpolation of the complex reflection coefficients at a given carrier frequency (using MATLAB's "griddedInterpolant" function) with a 30× finer voltage grid. These data were used to identify the maximum amplitude with full 360° phase coverage. Once that amplitude is known, operating points can be selected for various communications schemes. We collected data for BPSK, QPSK, and 16-QAM. Demonstration of 16-QAM is particularly interesting since it requires three different magnitude levels and 12 distinct phases, highlighting our independent phase and magnitude control. In each case, complex data points were selected for the scheme (e.g., four points with equal amplitude and 90° phase difference for QPSK), and the two bias voltages (one per layer) corresponding to those points were stored. We then created sequences of symbols by imposing those biasing pairs with the AWG.

Filtering and demodulation were then accomplished in postprocessing. The real and imaginary parts of the signal were measured separately and can be converted into a phase as a function of time, plotted in Fig. 14. The example of time data in Fig. 14 represents QPSK modulation with a symbol rate of 2 μs. Transition times are found to be substantially smaller, in the range of 0.05 μs ($-\pi/4 \rightarrow 3\pi/4$) to 0.25 μs ($3\pi/4 \rightarrow -3\pi/4$). We expect that these times are dictated by the voltage controller, the chosen trajectory in $[V_1, V_2]$ space, and the fan-out for the biasing network. As such, the system can be driven substantially faster and will likely not hit a limit until the voltage controller is optimized ($\sim$ 100 MHz). We leave further study of these limitations for future work but note that the metasurface

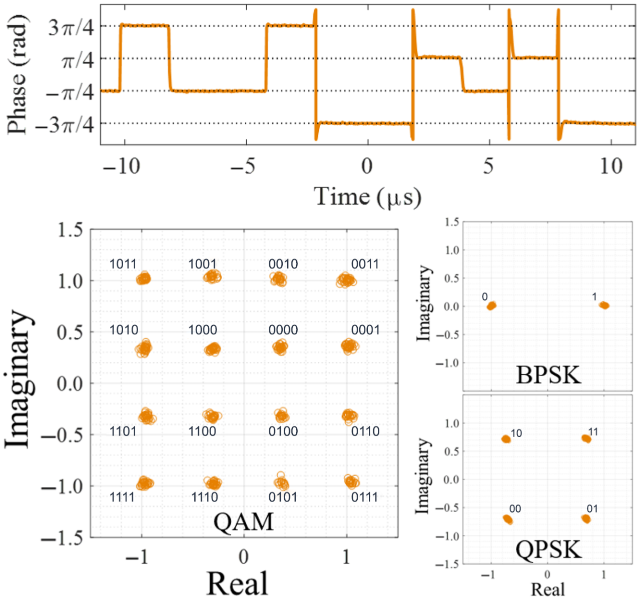

FIG. 14. Demonstration of communications with dynamic metasurface. The phase as a function of time is plotted, as well as the constellation diagrams for BPSK, QPSK, and QAM.

itself should theoretically support faster switching speeds. Further, more sophisticated demodulation techniques, e.g., equalization or error correction coding, can likely improve data transfer rates.

The process above was repeated for BPSK, QPSK, and 16-QAM. The symbol rate was maintained at $1/(2\ \mu\text{s}) = 500$ kHz, with the corresponding data rates increased by 2× and 4× for QPSK and 16-QAM, respectively. Constellation diagrams for these trials are shown in Fig. 14, and, as seen, there were no instances of bit errors over the thousands of bits encoded. To quantify the bit rate and bit error rate, a more exhaustive analysis must be undertaken, but the proof-of-concept experiment completed here effectively demonstrates the merit of the outlined approach. Ultimately we believe that symbol rates on the order of 10–100 MHz will be achievable with tailored voltage control and signal distribution. This requires high-frequency digital circuit design to drive a large quantity of capacitors and is therefore not the focal point of this paper. Ideally the varactors and the metasurface itself can be modulated on the order of hundreds of megahertz if voltage control and distribution are addressed, but this is left as a topic for future study.

IV. CONCLUSION

The wealth of applications for dynamic rf metasurfaces continues to spur their development. In this paper, we have proposed and demonstrated a dual-resonance unit cell that allows for independent control of magnitude and phase with two control voltages. Our metasurface was used to demonstrate communications and fits nicely with the rapidly emerging sixth-generation (6G) thrust toward reconfigurable intelligent surfaces. The independent magnitude and phase control is well suited for different modulation approaches, including QAM, which requires further study to understand the ultimate limitations.

Another interesting route for future research is to add spatial control to the metasurface so that the modulated signal can be redirected. This task is nontrivial since the biasing network must avoid interfering with the rf interactions that support the surfaces' behavior. With this spatial control, one could imagine inducing different phases across the surface while simultaneously crafting an amplitude taper—an enticing capability which enables control of sidelobes of reflected signals.

Aside from adding spatial control, it is also an interesting research avenue to imagine utilizing such a surface in a high-clutter, multipath, or cavity-like environment rather than in a free-space single-reflection setting. Such environments have been studied as architectures for deep learning [36] and can also be envisioned for advanced communications techniques, such as the covert communication technique demonstrated in Ref. [37].

Outside of the rf realm, these concepts can be of value across large portions of the electromagnetic spectrum. At lower frequencies, the form factor may become bulky but COTS components are abundantly available. Higher frequencies incur an additional challenge of materials science; however, we believe that, wherever single-layer dynamic metasurfaces show promise, the proposed techniques will also find purchase. This remains an interesting topic for future research especially as rf communications continue to expand in form and function.

The results demonstrated in this work are illustrative of the agile and robust capabilities that dynamic metasurface enable for communications applications and beyond. The presented design maintains a pragmatic form factor while at the same time delivering enhanced control over magnitude and phase. With the numerous applications and many avenues for continued basic research at hand, it is certain that cascaded dynamic metasurfaces will remain an area of great promise and interest.

[1] J. Gollub, O. Yurduseven, K. P. Trofatter, M. F. Imani, H. Odabasi, T. Sleasman, M. Boyarsky, T. Zvolensky, D. Arnitz, A. Pedross-Engel, G. Lipworth, A. Rose, D. R. Smith, M. Reynold, and D. Brady, Large metasurface aperture for millimeter wave computational imaging at the human-scale, Sci. Rep. **7**, 42650 (2017).

[2] N. Yuand and F. Capasso, Flat optics with designer metasurfaces, Nat. Mater. **13**, 139 (2014).

[3] H.-T. Chen, J. F. O'hara, A. K. Azad, A. J. Taylor, R. D. Averitt, D. B. Shrekenhamer, and W. J. Padilla,

Experimental demonstration of frequency-agile terahertz metamaterials, Nat. Photonics **2**, 295 (2008).

[4] T. Sleasman, M. F. Imani, J. N. Gollub, and D. R. Smith, Dynamic metamaterial aperture for microwave imaging, Appl. Phys. Lett. **107**, 204104 (2015).

[5] E. Basar, M. Di Renzo, J. De Rosny, M. Debbah, M.-S. Alouini, and R. Zhang, Wireless communications through reconfigurable intelligent surfaces, IEEE Access **7**, 116753 (2019).

[6] T. Sleasman, M. F. Imani, A. V. Diebold, M. Boyarsky, K. P. Trofatter, and D. R. Smith, Computational imaging with dynamic metasurfaces: A recipe for simple and low-cost microwave imaging, IEEE Antennas Propag. Mag. **64**, 123 (2022).

[7] R. Schmid, D. Shrekenhamer, O. Somerlock, A. Malone, T. Sleasman, and R. Awadallah, in *2020 IEEE Radio and Wireless Symposium (RWS)* (IEEE, San Antonio, Texas, 2020), p. 91.

[8] K. Chen, Y. Feng, F. Monticone, J. Zhao, B. Zhu, T. Jiang, L. Zhang, Y. Kim, X. Ding, S. Zhang, *et al.*, A reconfigurable active Huygens' metalens, Adv. Mater. **29**, 1606422 (2017).

[9] H. Zhang, N. Shlezinger, F. Guidi, D. Dardari, M. F. Imani, and Y. C. Eldar, in *2022 IEEE 23rd International Workshop on Signal Processing Advances in Wireless Communication (SPAWC)* (IEEE, Oulu, Finland, 2022), p. 1.

[10] L. Liu, C. Caloz, and T. Itoh, Dominant mode leaky-wave antenna with backfire-to-endfire scanning capability, Electron. Lett. **38**, 1 (2002).

[11] H. Zhu, S. Cheung, X. Liu, and T. Yuk, Design of polarization reconfigurable antenna using metasurface, IEEE Trans. Antennas Propag. **62**, 2891 (2014).

[12] C. L. Holloway, E. F. Kuester, and A. Dienstfrey, Characterizing metasurfaces/metafilms: The connection between surface susceptibilities and effective material properties, IEEE Antennas Wirel. Propag. Lett. **10**, 1507 (2011).

[13] C. L. Holloway, E. F. Kuester, J. Gordon, J. O. Hara, J. Booth, and D. R. Smith, An overview of the theory and applications of metasurfaces: The two-dimensional equivalents of metamaterials, IEEE Antennas Propag. Mag. **54**, 10 (2012).

[14] C. Pfeifferand and A. Grbic, Cascaded metasurfaces for complete phase and polarization control, Appl. Phys. Lett. **102**, 231116 (2013).

[15] C. Pfeifferand and A. Grbic, Metamaterial Huygens' Surfaces: Tailoring Wave Fronts with Reflectionless Sheets, Phys. Rev. Lett. **110**, 197401 (2013).

[16] B. Zheng, H. Ren, S. An, H. Tang, H. Li, M. Haerinia, Y. Dong, C. Fowler, and H. Zhang, Tunable metasurface with dynamic amplitude and phase control, IEEE Access **9**, 104522 (2021).

[17] J. Zhang, X. Wei, I. D. Rukhlenko, H.-T. Chen, and W. Zhu, Electrically tunable metasurface with independent frequency and amplitude modulations, ACS Photonics **7**, 265 (2020).

[18] M. Liu, W. Zhu, P. Huo, L. Feng, M. Song, C. Zhang, L. Chen, H. J. Lezec, Y. Lu, A. Agrawal, *et al.*, Multifunctional metasurfaces enabled by simultaneous and independent control of phase and amplitude for orthogonal polarization states, Light Sci. Appl. **10**, 1 (2021).

[19] L. Liu, X. Zhang, M. Kenney, X. Su, N. Xu, C. Ouyang, Y. Shi, J. Han, W. Zhang, and S. Zhang, Broadband metasurfaces with simultaneous control of phase and amplitude, Adv. Mater. **26**, 5031 (2014).

[20] L. Bao, Q. Ma, G. D. Bai, H. B. Jing, R. Y. Wu, X. Fu, C. Yang, J. Wu, and T. J. Cui, Design of digital coding metasurfaces with independent controls of phase and amplitude responses, Appl. Phys. Lett. **113**, 063502 (2018).

[21] M. Z. Chen, W. Tang, J. Y. Dai, J. C. Ke, L. Zhang, C. Zhang, J. Yang, L. Li, Q. Cheng, S. Jin, *et al.*, Accurate and broadband manipulations of harmonic amplitudes and phases to reach 256 QAM millimeter-wave wireless communications by time-domain digital coding metasurface, Natl. Sci. Rev. **9**, nwab134 (2022).

[22] T. Sleasman, M. Boyarsky, M. Imani, J. Gollub, and D. Smith, Design considerations for a dynamic metamaterial aperture for computational imaging at microwave frequencies, JOSA B **33**, 1098 (2016).

[23] T. Sleasman, M. F. Imani, J. N. Gollub, and D. R. Smith, Microwave Imaging Using a Disordered Cavity with a Dynamically Tunable Impedance Surface, Phys. Rev. Appl. **6**, 054019 (2016).

[24] M. Boyarsky, T. Sleasman, M. F. Imani, J. N. Gollub, and D. R. Smith, Electronically steered metasurface antenna, Sci. Rep. **11**, 1 (2021).

[25] N. Landy, J. Hunt, and D. R. Smith, Homogenization analysis of complementary waveguide metamaterials, Photonics Nanostruct. - Fundam. Appl. **11**, 453 (2013).

[26] C. R. Simovskiand and S. A. Tretyakov, Local constitutive parameters of metamaterials from an effective-medium perspective, Phys. Rev. B **75**, 195111 (2007).

[27] D. Sievenpiper, L. Zhang, R. F. J. Broas, N. G. Alexopolous, and E. Yablonovitch, High-impedance electromagnetic surfaces with a forbidden frequency band, IEEE Trans. Microw. Theory Tech. **47**, 2059 (1999).

[28] D. F. Sievenpiper, J. H. Schaffner, H. J. Song, R. Y. Loo, and G. Tangonan, Two-dimensional beam steering using an electrically tunable impedance surface, IEEE Trans. Antennas Propag. **51**, 2713 (2003).

[29] N. Kaina, M. Dupré, M. Fink, and G. Lerosey, Hybridized resonances to design tunable binary phase metasurface unit cells, Opt. Express **22**, 18881 (2014).

[30] S. Tretyakov*Analytical Modeling in Advanced Electromagnetics* (Artech House, Norwood, MA, 2003).

[31] T. R. Cameronand and G. V. Eleftheriades, Analysis and characterization of a wide-angle impedance matching metasurface for dipole phased arrays, IEEE Trans. Antennas Propag. **63**, 3928 (2015).

[32] A. Olkand and D. Powell, Accurate Metasurface Synthesis Incorporating Near-Field Coupling Effects, Phys. Rev. Appl. **11**, 064007 (2019).

[33] H. Hausand and W. Huang, Coupled-mode theory, Proc. IEEE **79**, 1505 (1991).

[34] W. Suh, Z. Wang, and S. Fan, Temporal coupled-mode theory and the presence of non-orthogonal modes in lossless multimode cavities, IEEE. J. Quantum Electron. **40**, 1511 (2004).

[35] Comsol multiphysics, www.comsol.com.

[36] B. W. Frazier, T. M. Antonsen Jr, S. M. Anlage, and E. Ott, Deep-Learning Estimation of Complex Reverberant Wave Fields with a Programmable Metasurface, Phys. Rev. Appl. **17**, 024027 (2022).

[37] M. F. Imani, D. R. Smith, and P. del Hougne, Perfect absorption in a disordered medium with programmable meta-atom inclusions, Adv. Funct. Mater. **30**, 2005310 (2020).